communications materials

A Nature Portfolio journal

Article

https://doi.org/10.1038/s43246-026-01135-8

Mean field magnetism and spin frustration in a double perovskite oxide with compositional complexity

Nandana Bhattacharya[1] ✉, Ravi Kiran Dokala[2], Sourav Chowdhury[3], Suresh Chandra Joshi[1], Subha Dey[1], Jayjit Kumar Dey[3], Subhajit Nandy[3], Daniel Pérez-Salinas[4], Manuel Valvidares[4], Moritz Hoesch[3], Roland Mathieu[2] & Srimanta Middey[1] ✉

With the rise of high entropy oxides, compositional disorder has emerged as a powerful tuning parameter for oxide-based functional properties, prompting the study of its influence on long-range magnetic ordering in double perovskite systems. In this work, we consider the RE_2NiMnO_6 (*RE* : rare-earth) family and investigate single-crystalline films of $(La_{0.4}Nd_{0.4}Sm_{0.4}Gd_{0.4}Y_{0.4})NiMnO_6$. Despite configurational disorder and high cationic size variance at the *RE*-site, the material exhibits robust ferromagnetic ordering with a Curie temperature (T_c) of approximately 150 K, consistent with expectations based on the average ionic radii of the *RE*-sites in bulk RE_2NiMnO_6 family. Below T_c, Raman spectroscopy reveals deviations from anharmonic behavior, where the phonon renormalization aligns with a mean-field approximation of spin-spin correlation. At lower temperature, magnetic *RE* ions contribute to the magnetic behavior, and the system displays a reentrant spin-glass-like behavior. This study demonstrates that while a mean-field approach viably captures the long-range transition temperature, microscopic magnetic interactions are essential for understanding the low-temperature phase.

Transition metal oxides are a fertile ground for a wide array of magnetic phases, from long-range ordered phases like ferromagnetism, antiferromagnetism[1], altermagnetism[2,3] to frustrated states such as spin-glass[4] and spin-liquid[5]. This rich magnetism, along with its coupling to underlying lattice, orbital, and charge degrees of freedom, give rise to fascinating magnetic phenomena such as colossal magnetoresistance[6], skyrmions[7], anomalous Hall effect[8], topological Hall effect, etc[9,10]. Modern condensed matter physics often focuses on engineering these properties in thin film form by controlling strain, confinement, heterointerfaces, geometrical lattice engineering, etc.[11,12]. In recent years, high entropy oxides (HEOs) containing five or more number of elements are being investigated as a new paradigm of materials design, providing several advantages over traditional materials[13–24]. While conventional notion suggests that such compositional disorder would disrupt magnetic interactions and favor a spin-glass-like phase or inhomogeneous magnetic phase[25–29], a surprising number of magnetic HEOs exhibit long-range magnetism[30–36]. This raises a fundamental question: How can we describe the magnetism in these systems? Instead of focusing on microscopic variations [Fig. 1(a), (b)], could a mean-field approach[37], which considers an average internal magnetic field around each magnetic moment, be a suitable starting point for understanding their magnetic behavior? To examine this, we focus on an insulating double perovskite oxide in this work.

Double perovskite oxides (DPOs) with the general formula $A_2BB'O_6$ (where *B*, *B′* are transition metal (TM) cations) show a variety of magnetic ground states owing to their structural flexibility and the possibility of incorporating two distinct TM cations[38]. In this work, we consider the RE_2NiMnO_6 family (*RE*= La, Pr, Nd,...,Y), which shows a transition from paramagnetic insulating to ferromagnetic insulating phase upon lowering the temperature[39–43]. Due to their potential for use in low-power, energy-efficient spintronic devices, ferromagnetic insulators (FMIs) are a subject of significant research interest. This has led to a push for the development of transition-metal-oxide-based FMIs, facilitated by recent advances in oxide thin-film growth techniques[44,45]. In the RE_2NiMnO_6 series of FMIs, the ferromagnetic ordering is caused by Ni^{2+}-O-Mn^{4+} ferromagnetic super-exchange, and the transition temperature (T_c) strongly depends on the choice of *RE*ion (Table 1)[46]. The magnetic interactions between the *RE*-sites

[1]Department of Physics, Indian Institute of Science, Bengaluru, India. [2]Department of Materials Science and Engineering, Uppsala University, Box 35, 751 03 Uppsala, Sweden. [3]Deutsches Elektronen-Synchrotron DESY, Hamburg, Germany. [4]ALBA Synchrotron Light Source, Cerdanyola del Valles, Barcelona, Spain. ✉e-mail: nandanab@iisc.ac.in; smiddey@iisc.ac.in

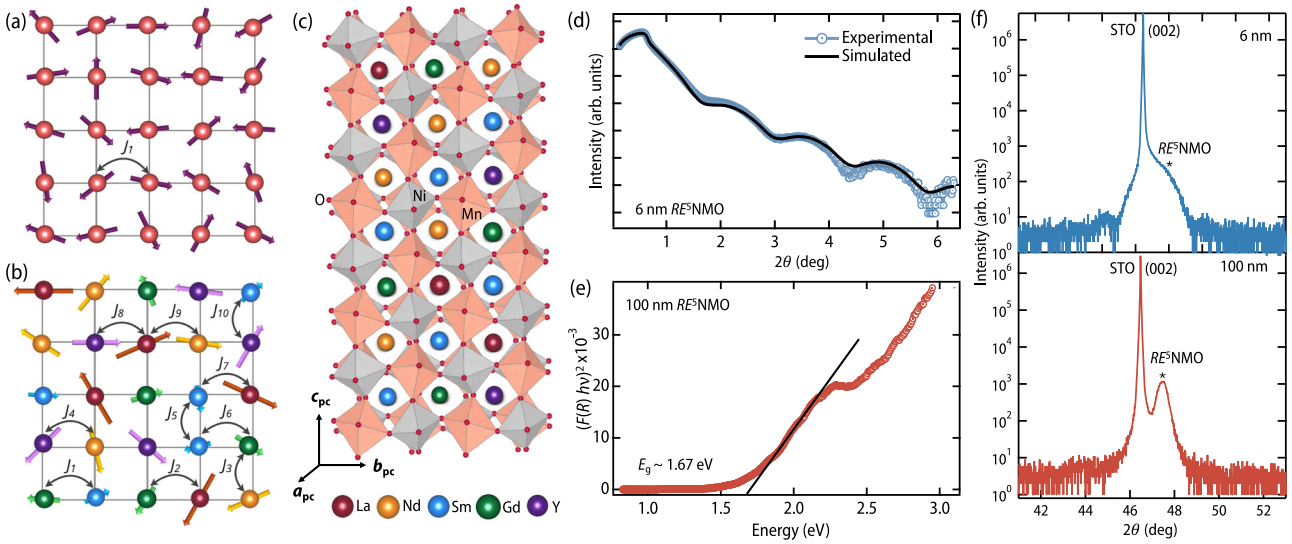

Fig. 1 | Film characterization and electronic structure. Schematic depicting the exchange coupling in a square lattice with **a** one kind of atom exhibiting uniform nearest neighbor interactions **b** random distribution of five different kinds of atoms with different nearest neighbor couplings. **c** Crystal structure of an Ni-Mn ordered RE^5NMO where the *A*-site is shown for a random distribution of 5 *RE* cations [Legend for colors representing each *RE* cation has been shown at the bottom]. **d** Experimental XRR data and corresponding footprint-corrected, GenX-based model fitting for a 6 nm RE^5NMO film on STO substrate, showing well-defined Kiessig fringes. **e** The reflectance data were used to derive the Kubelka-Munk function, which is an absorption equivalent commonly used for the diffused reflectance mode given by, $F(R) = (1\text{-}R^2) / 2R$, where R is the reflectance[90]. The Tauc relation using the reflectance mode is given by $[[F(R) \cdot h\nu]^n = A(h\nu - E_g)]$ where, $F(R)$ is the Kubelka-Munk function described above, A is a characteristic constant independent of the photon energy, $h\nu$ is the photon energy and E_g is the band gap[55]. We use $n = 2$ here as RE_2NiMnO_6 exhibit direct optical band gaps[91,92]. The black line is the linear extrapolation for the Tauc plot to find the band gap. **f** XRD for 6 nm (upper panel) and 100 nm (lower panel) RE^5NMO film on STO, * denotes the film peak. While the overlap of the substrate and film prohibits the estimation of the out-of-plane pseudocubic lattice parameter (c_{pc}) for the 6 nm film, it is found to be ~ 3.83 Å for the 100 nm film.

Table 1 | Electronic configuration, magnetic moments, and ionic radii of RE^{3+} cations and corresponding magnetic transitions in RE_2NiMnO_6 compounds

RE^{3+}	Electronic configuration	*L*	*S*	Ground-state term $^{2S+1}L_J$	Effective *RE* moment $\mu_J = g_J\sqrt{J(J+1)}\,\mu_B$	Ionic radii (Å) 89	RE_2NiMnO_6	T_c (K) 46
La^{3+}	$4f^0$	0	0	$^1S_0$	0	1.160	La_2NiMnO_6	270
Pr^{3+}	$4f^2$	5	1	$^3H_4$	3.58	1.126	Pr_2NiMnO_6	212
Nd^{3+}	$4f^3$	6	3/2	$^4I_{9/2}$	3.62	1.109	Nd_2NiMnO_6	194
Sm^{3+}	$4f^5$	5	5/2	$^6H_{5/2}$	0.84	1.079	Sm_2NiMnO_6	157
Eu^{3+}	$4f^6$	3	3	$^7F_0$	0	1.066	Eu_2NiMnO_6	143
Gd^{3+}	$4f^7$	0	7/2	$^8S_{7/2}$	7.94	1.053	Gd_2NiMnO_6	128
Tb^{3+}	$4f^8$	3	3	$^7F_6$	9.72	1.040	Tb_2NiMnO_6	111
Dy^{3+}	$4f^9$	5	5/2	$^6H_{15/2}$	10.63	1.027	Dy_2NiMnO_6	93
Ho^{3+}	$4f^{10}$	6	2	$^5I_8$	10.60	1.015	Ho_2NiMnO_6	82
Y^{3+}	$4d^0$	0	0	$^1S_0$	0	1.019	Y_2NiMnO_6	79

and the Ni/Mn sublattice have also been reported[41,46,47]. To examine the effect of compositional complexity under a high-entropy setting, we examine $(La_{0.4}Nd_{0.4}Sm_{0.4}Gd_{0.4}Y_{0.4})NiMnO_6$ (RE^5NMO) [See Fig. 1(c) for schematic depiction]. The choice of this particular combination of *RE* ions is motivated to obtain a high cationic variance at the *RE*-site ($\sigma^2 = \sum_{i=1}^{n} y_i r_i^2 - < r_A >^2 \sim 23.3\ pm^2$, where r_i is the cationic radius with fractional occupancy y_i, and $< r_A >$ is the mean radius[23]). This high-variance regime is of particular interest for understanding the physical properties of HEOs, as a recent study on their electronic behavior has shown variance-induced decoupling of otherwise simultaneous transitions, leading to an emergent phase which is not obtained in low-variance $RENiO_3$-based systems[23,36,48–50]. In this regard, the understanding of how magnetic order responds to high variance remains largely unexplored.

In this study, single-crystalline films of RE^5NMO were grown on $SrTiO_3$ (001) substrates via pulsed laser deposition (PLD). DC magnetometry measurements on a 100 nm film revealed a robust ferromagnetic transition with a T_c of approximately 150 K. This T_c is notably close to that reported for Sm_2NiMnO_6[46], implying that the net ferromagnetic exchange is primarily governed by the average bond angles, which, in turn, are controlled by the size of the *RE* ions. Raman spectroscopy revealed a clear deviation in the phonon frequency from the anharmonic model observed below T_c. Intriguingly, this deviation, occurring just below T_c, could be accounted for by considering a mean-field model of magnetism[51]. However, a distinct magnetic anomaly emerged near 35 K, below which the mean-field model failed to describe the system's behavior, and the system exhibited reentrant spin glass-like behavior. Although both Ni-Mn antisite disorder (ASD) as well as *RE*-site magnetic disorder are deemed to be the drivers of this spin glass state, the transition temperature is markedly lower than the ASD driven transitions reported in parent *RE* compounds[40,52–54] and surprisingly matches the *RE* interaction temperature scale.

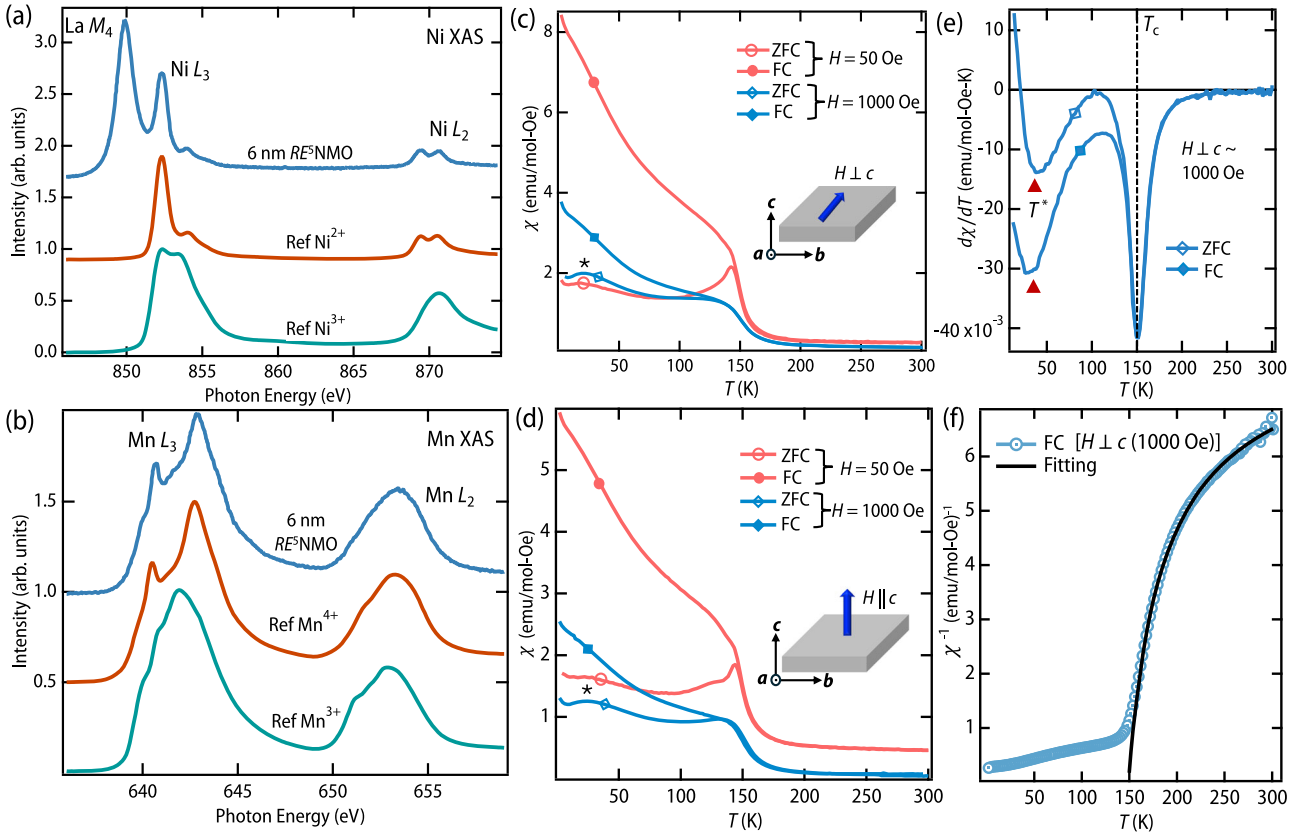

Fig. 2 | Long range magnetic ordering. XAS spectra for **a** Ni $L_{3,2}$ edge; Inset : zoomed L_2 edge highlighting the characteristic Ni^{2+} splitting, and **b** Mn $L_{3,2}$ edge. The reference for Ni^{2+}, Ni^{3+}, Mn^{3+} and Mn^{4+} have been shown for ease of comparison. χ vs T for both ZFC and FC conditions recorded in the warming and cooling cycles, respectively, under fields of 50 Oe and 1000 Oe applied **c** in-plane to the film ($H \perp c$) **d** out-of-plane to the film ($H \parallel c$), where c is the out-of-plane crystallographic direction. The schematic of the measurement geometry have been shown in the inset. **e** Temperature derivative of susceptibility, $d\chi/dT$, under 1000 Oe ($H \perp c$), highlighting the Curie temperature (T_c) and lower temperature anomaly (marked by arrow, T^*). **f** χ^{-1} as a function of temperature for $H \perp c$ under 1000 Oe, fitted with a modified Curie-Weiss formula (black curve).

Results

Film growth and characterizations

RE^5NMO films have been grown on $SrTiO_3$ [001] (STO) substrates by a Neocera PLD system (growth parameter details are in Methods section). The structural quality of the films have been verified by X-ray reflectivity (XRR) and X-ray diffraction (XRD) measurements using a laboratory-based diffractometer. The presence of prominent intensity oscillations across the entire scan range in the XRR pattern [Fig. 1(d)] is indicative of a highly crystalline nature with a smooth interface [See inset Supplementary Fig. S2 for the XRR of 100 nm film]. The fitting results yielded a film thickness ~ 6 nm and a film/substrate roughness of about 3.7 Å. The laser pulse calibration obtained from the above analysis was further used for the growth of the 100 nm film. Figure 1(f) shows the XRD patterns for the 6 nm and 100 nm films, both of which contain a broad film peak next to the sharp substrate peak, confirming their single-crystallinity. The long-range XRD scan for the 100 nm film further confirms the phase purity of the film with no detectable secondary phase [See Supplementary Fig. S2]. The rocking curve XRD of $(002)_{pc}$ for the 100 nm film finds a bimodal structural character: a sharp epitaxial component [full width at half maxima (FWHM) ~ 0.08°], associated with the coherently strained region near the film-substrate interface, and a broader component (FWHM ~1°), attributed to strain-relaxed layers [Inset, Supplementary Fig. S2]. The structural relaxation may arise due to a combination of high variance-driven lattice distortions and change in growth dynamics in high thickness regime. Future study involving the measurement of coherent Bragg rods using synchrotron radiation and atomically resolved electron microscopy for films with different thickness will be necessary to understand this aspect[48].

We further characterized the film through the determination of the optical band gap by measuring the diffuse reflectance spectrum and the Tauc plot analysis[55]. The optical band gap E_g is found to be ~ 1.67 eV [Fig. 1(e)] for the 100 nm film, which is comparable to the parent members of the RE_2NiMnO_6 family[43].

The origin of ferromagnetism in the parent RE_2NiMnO_6 series has been explained by the dominance of the ferromagnetic (FM) superexchange interaction between Ni^{2+}-e_g and Mn^{4+}-e_g states over the antiferromagnetic (AFM) superexchange between half-filled Ni^{2+}-e_g and Mn^{4+}-t_{2g} orbitals[56]. The presence of unwanted Ni^{3+} and Mn^{3+} can give rise to additional magnetic transition at lower temperature[52]. To examine this, we performed the X-ray absorption spectroscopy (XAS) experiments on Ni $L_{3,2}$ [Fig. 2(a)] and Mn $L_{3,2}$ [Fig. 2(b)] edges on our 6 nm film at P04 beamline, PETRA III, DESY, using total electron yield (TEY) mode. Reference spectra of a 20 uc $Nd_2Ni^{2+}Mn^{4+}O_6$[57], $NdNi^{3+}O_3$, and $NdMn^{3+}O_3$ films grown on $NdGaO_3$ have also been shown for comparison. The Ni L_3 spectra are also overlapped with the La M_4 spectral feature. As shown in Fig. 2(a), (b), the Ni and Mn spectral features of the film clearly confirm +2 and +4 oxidation states, respectively, similar to oxidation states reported for the bulk parent compounds of RE_2NiMnO_6 (RE = La, Nd, Sm, Gd and Y)[41,43,58]. A weak spectral feature around 639 eV is observed in the Mn XAS and is attributed to Mn^{2+} surface states. Such features are commonly reported for the top ~ 1–2 unit cell surface layers of epitaxial manganite films and originate from surface symmetry breaking associated with the absence of apical oxygen[57,59–62]. Recent studies of Nd_2NiMnO_6 films grown on $SrTiO_3$ (001) substrates have reported a change in the oxidation state of Mn due to polar catastrophe, while Ni remains in its +2 oxidation state[57,63]. The contribution of both the

surface and polar catastrophe effects is insignificant in the film thickness regime we are probing in this work[63].

Ferromagnetic ordering and validity of a mean field model

After confirming the desired oxidation state of Ni and Mn, we focus on investigating the magnetic properties. The magnetic superexchange coupling (J) is dependent on the Ni^{2+}-O-Mn^{4+} bond angle ($J \propto \cos^2\theta$)[56], which in turn is dependent on the ionic radii of the *RE* cations, leading to a correlation between the *RE* ionic radii and magnetic transition temperature T_c[46]. To probe the effect of compositional complexity at the *RE* site on the magnetism, we employed SQUID magnetometry on the 100 nm film. The measurements have been performed in both in-plane (perpendicular to the crystallographic c-axis, $H \perp c$) and out-of-plane directions (parallel to c -axis, $H \parallel c$) with respect to the film geometry [Inset Fig. 2(c), (d), respectively]. Figure 2(c) and (d) show the zero field cooled (ZFC) and field cooled (FC) dc susceptibility ($\chi = M/H$) measured in warming cycle and cooling cycle, respectively, for RE^5NMO under magnetic fields of 50 Oe and 1000 Oe. A clear bifurcation between the FC and ZFC magnetization curves is observed around 150 K, particularly prominent for the lower field (50 Oe). Such behavior is indicative of the onset of long-range ferromagnetic ordering[41,64]. The derivative of susceptibility ($d\chi/dT$) also finds the $T_c \sim 150$ K [Fig. 2(e) and Supplementary Fig. S3].

Amongst the parent counterparts, in Nd_2NiMnO_6, Sm_2NiMnO_6, and Gd_2NiMnO_6, interactions between the *RE* moments and the Ni/Mn sublattice give rise to distinct low temperature anomalies in the FC M-T curves[41,46]. Interestingly, the ZFC magnetization curves exhibit a broad, cusp-like anomaly marked as * in Fig. 2(c), (d) for both measurement orientations [also observed in $d\chi/dT \sim 35$ K marked as T^* in Fig. 2(e)]. Such a feature is often associated with the onset of a glassy state, where competing magnetic interactions lead to magnetic frustration[40,64,65], which shall be demonstrated and discussed in greater detail in a latter section of this paper.

In Fig. 2(f), we show the fitting of the inverse of susceptibility using a modified Curie-Weiss model assuming a non-interacting nature of the *RE* moments at higher temperature:

$$\chi(T) = \chi_0 + \frac{C_{RE}}{T} + \frac{C_{\mathrm{Ni-Mn}}}{T - \theta_{\mathrm{CW}}}$$

where χ_0 is the Van-Vleck paramagnetic susceptibility, C_{RE} and $C_{\mathrm{Ni\text{-}Mn}}$ are the Curie constants for the *RE* and the Ni/Mn sublattices, respectively, and θ_{CW} is the Curie-Weiss temperature[37,46]. We fixed the value of C_{RE} during the fitting procedure by estimating the average effective magnetic moment of the *RE* sublattice using the root-mean-square formula: $\mu_{\mathrm{eff,RE}} = \sqrt{\sum_i x_i \mu_i^2}$ (x_i is the atomic fraction and μ_i is the effective moment of the i^{th}*RE* atom), which yields $\mu_{\mathrm{eff},RE} \approx 3.9\mu_B$. This value was then related to the Curie constant via the relation $\mu_{\mathrm{eff}} = \sqrt{8C_{RE}}$[64]. From the relation $\mu_{\mathrm{eff}} = \sqrt{\sum g_i^2 S_i(S_i+1)}$, for Ni^{2+} (d^8, S= 1) and Mn^{4+} (d^3, S =3/2), assuming g = 2 and g = 2.5 for Mn and Ni, respectively[46,66], the effective moment for the Ni-Mn network should be 5.24 μ_B. Our analysis yields $C_{\mathrm{Ni\text{-}Mn}} \sim 5.98\ \mu_B$, close to the expected value. Furthermore, a $\theta_{\mathrm{CW}} \sim 149$ K is obtained, very close to the T_c found from the results discussed in Fig. 2(c), (d). The positive value of θ_{CW} and the fact that $T_c \approx \theta_{\mathrm{CW}}$ further corroborate that the magnetic transition in our system is ferromagnetic in nature, without any significant role of magnetic frustration effect at higher temperatures. Most importantly, the T_c and θ_{CW} are closer to that of parent Sm_2NiMnO_6, which share the similar average tolerance factor. These results affirm that the ferromagnetic transition temperature, despite the compositional complex setting at the *RE* sublattice with large variance, is governed in a mean-field way. This is further examined through Raman spectroscopy.

Correlating magnetism to phonon vibrations

In FMI DPOs, the ferromagnetic ordering has been shown to exhibit a pronounced effect on the phonon frequencies below T_c owing to strong spin-phonon coupling[43,51,67]. In the backdrop of the possibility of having different types of *RE* ions surrounding a particular Ni/Mn site, we next investigate the structure-magnetism correlation using Raman spectroscopy as a function of temperature (measurement details are in the Methods section). For the entire range of temperature (300 K to 4.2 K), we observe two prominent Raman modes in the range of 400 to 800 cm^{-1} phonon frequencies [Supplementary Fig. S5(a)]: ~ 510 and 653 cm^{-1}, consistent with previous reports for monoclinic RE_2NiMnO_6[43,51,68], also affirming the absence of any structural transitions.

Since the B_g Raman mode ~ 510 cm^{-1} has strong contribution from the STO substrate [Supplementary Fig. S5(b) for temperature dependent Raman spectra for STO substrate] with increase in temperature, we focus on the analysis of Raman mode around 653 cm^{-1} [Fig. 3(a)], which is assigned to the symmetric A_g stretching vibration of the BO_6 octahedra (B = Ni, Mn) and is highly sensitive to changes in the lattice dynamics and magnetic order[67–69]. The spectra were fitted with two Lorentzian functions, and the fitted curves are shown in Fig. 3(a): one to capture the A_g Raman mode, and another, smaller peak at a lower frequency ~ 618 cm^{-1} [See Supplementary Fig. S6] to capture the monoclinic distortion[68] and/or contribution from STO substrate since both overlap at similar phonon frequencies. The extracted A_g mode peak phonon frequencies are plotted as a function of temperature [Fig. 3]. Further analysis of this mode revealed that the mode frequency above T_c fit well with the standard Balkanski model for anharmonic temperature dependence given by,

$$\omega(T) = \omega_0 - C\left(1 + \frac{2}{e^{\hbar\omega_0/2k_BT} - 1}\right) \quad (1)$$

where $\omega(T)$ is the phonon frequency at temperature T, ω_0 is the phonon frequency at $T = 0$ K, and C is the anharmonic constant[67,70]. A stark deviation from the anharmonic model and softening of the A_g phonon mode is observed below 150 K that corresponds to the T_c found from our magnetization measurements. Such softening has been shown to emanate from magnetic order-induced phonon-renormalization, a clear indicator of strong spin-phonon coupling in the system in the magnetically ordered phase, as has also been observed in the parent RE_2NiMnO_6 compounds[51,68].

Within the molecular field approximation, such phonon renormalization is proportional to the spin-spin correlation function $\langle \vec{S}_i \cdot \vec{S}_j \rangle$ for nearest-neighbor localized spins[71]. In case of ferromagnetic interaction under mean field approximation, $\langle \vec{S}_i \cdot \vec{S}_j \rangle$ is proportional to $M(T)^2$ giving $\Delta\omega(T) = \omega(T) - \omega_{\mathrm{anh}}(T) \propto -M^2(T)/M^2_{\mathrm{max}}$[67–69]. As shown in Fig. 3(c), the phonon frequency shift $\Delta\omega(T) = \omega(T) - \omega_{\mathrm{anh}}(T)$ is plotted alongside the normalized square of magnetization term, $-M^2(T)/M^2_{\mathrm{max}}$ which is derived from the M–T measurements shown in Fig. 2(c). The close correspondence between these two curves around T_c confirms that the anomalous phonon softening originates from the spin-phonon coupling in the ferromagnetic phase and further validates a mean field description of the magnetism[67,68,72]. Interestingly, we observe a deviation from this mean-field behavior at lower temperatures, similar to the magnetic anomaly observed in the ZFC measurements.

Isothermal magnetization versus field and nature of magnetic couplings

We also performed isothermal $M-H$ measurements at selected temperatures below T_c. Figure 4(a) displays $M-H$ loops at 2, 10, 50, and 100 K for $H \perp c$ [See Supplementary Fig. S3 for $H \parallel c$ results]. We observe a well-defined hysteresis loop consistent with the ferromagnetic behavior. However, we do not observe any significant perpendicular magnetic anisotropy in the present case [See Supplementary Fig. S3 for comparison of $M-H$ at 10 K and 50 K for both $H \perp c$ and $H \parallel c$]. Starting with the highest temperature 100 K [Fig. 4(a)], the $M-H$ curve exhibits soft ferromagnetism with a coercivity ~ 200 Oe. The magnetization at higher fields shows a near saturation at about 1 μ_B/f.u. (f.u. = formulae unit), and 1.6 μ_B/f.u. for 100 K, and 50 K, respectively. Conventionally, on lowering the temperature, it is expected to be a clearer saturation of magnetization with an enhancement of the coercive field (H_c). While the H_c increases to ~ 1200 Oe for 2 K, we find an increasing non-saturating trend of M at higher H. To probe this peculiar

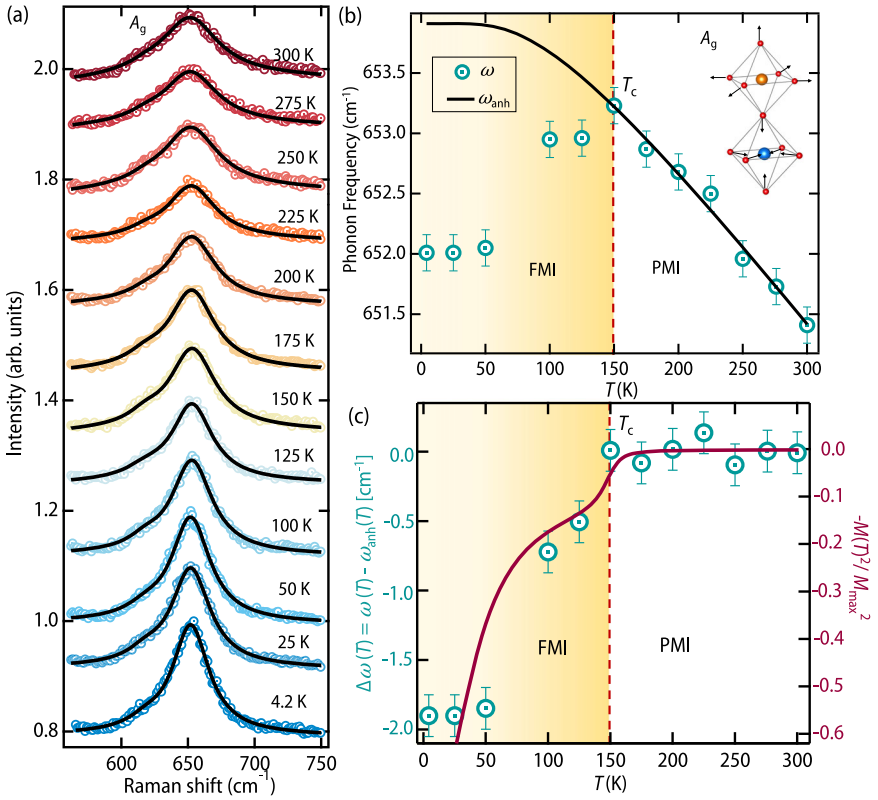

Fig. 3 | Temperature dependence of A_g raman mode. a Temperature-dependent Raman spectra of RE^5NMO measured from 4.2 K to 300 K, showing the evolution of the A_g phonon mode. **b** Temperature dependence of the A_g mode peak position, fitted using an anharmonic phonon decay model (black curve). The error bar in fitting of the Raman spectra is 0.15 cm^{-1}. FMI and PMI represent ferromagnetic insulating and paramagnetic insulating states respectively. **c** Comparison of phonon frequency shift $\Delta\omega(T)$, obtained by subtracting the peak positions derived from Lorentzian fitting, from the values obtained from anharmonic model, with $M^2(T)/M^2_{max}$.

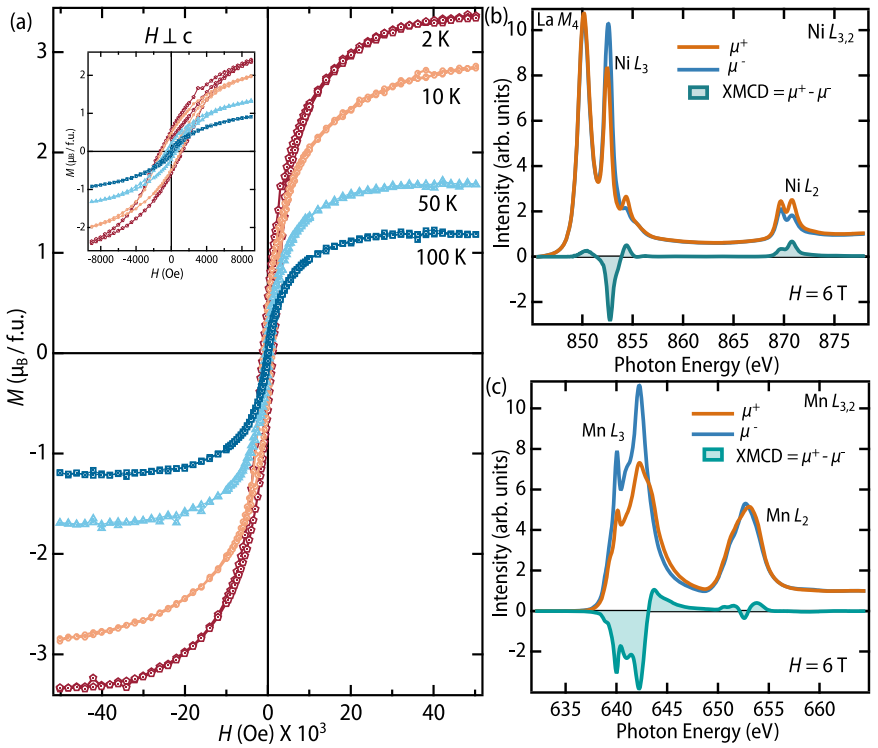

Fig. 4 | Ferromagnetic hysteresis and Ni/Mn coupling. a M-H curves at 2 K, 10 K, 50 K, and 100 K for $H \perp c$. Inset: Corresponding zoomed M-H curves highlighting the hysteresis. Right and left circularly polarized XAS spectra (denoted by μ^+ and μ^- respectively) along with their difference XMCD signal at **b** Ni $L_{3,2}$ and **c** Mn $L_{3,2}$ edge exhibiting ferromagnetic coupling.

behavior, we perform element-specific X-ray magnetic circular dichroism (XMCD) measurements at both the TM and *RE* cation edges, crucial for the determination of the magnitude and alignment of their individual spin and orbital magnetic moments[73,74].

We first examine the coupling between the Ni and Mn sites from their respective XMCD signal obtained by the difference between the right and left circularly polarized absorption spectra (μ^+ -μ^-) [Fig. 4(b), (c)]. All spectra were measured at the BOREAS beamline of the ALBA synchrotron, Spain, under a magnetic field of 6 T and temperature of 2 K, in grazing incidence geometry [See Methods for details]. The sign of the leading edge of the XMCD with the relatively larger spectral weight is dictated by the spin magnetic moment (m_s)[41,75]. From the negative sign of the XMCD leading

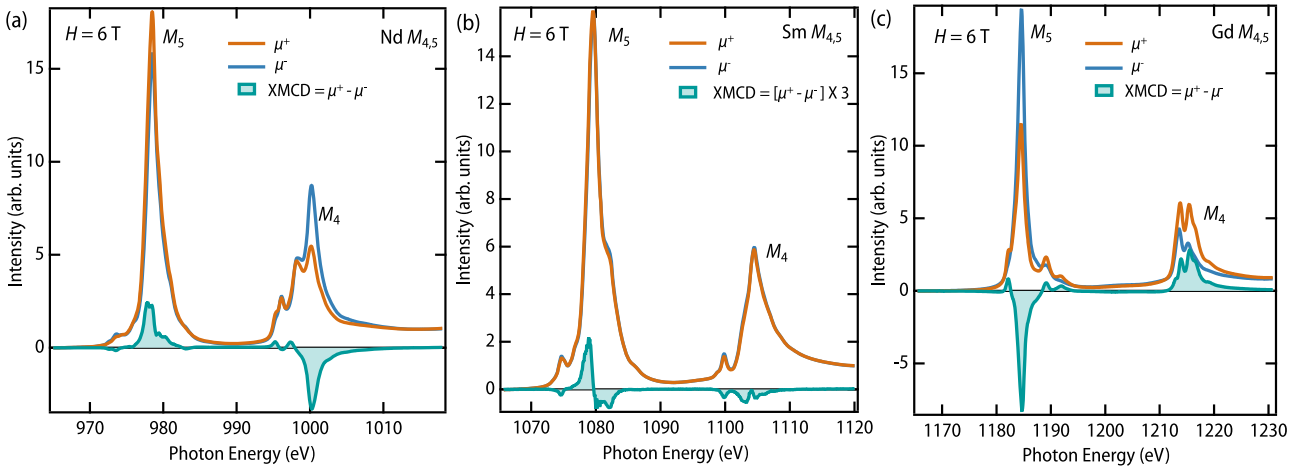

Fig. 5 | XMCD at *RE* edges. Right and left circularly polarized XAS spectra measured under 6 Tesla magnetic field for the *RE* edges, along with their difference XMCD signal at **a** Nd $M_{4,5}$, **b** Sm $M_{4,5}$, and **c** Gd $M_{4,5}$ edges.

edge for both the Ni and Mn spectra, we confirm the ferromagnetic coupling between the Ni and Mn cations akin to the parent compounds, with m_s aligned in the direction of the field[41,58,63]. Sum-rule analysis of the XMCD signal[76,77] at the Mn $L_{3,2}$ edge [see Supplementary Note 7 for calculation details] yielded a spin moment $m_s \approx 2.11\ \mu_B$ and an orbital moment $m_l \approx 0.08\ \mu_B$, consistent with the expected quenching of orbital angular momentum in 3*d* cations[63]. This m_s is much smaller compared to the expected theoretical value of 3.87 μ_B for Mn^{4+} [S = 3/2]. The reduction is related to the Ni-Mn ASD, which introduced antiferromagnetic Mn^{4+}-O-Mn^{4+} and Ni^{2+}-O-Ni^{2+} couplings[58,78]. Due to the overlap between the La M_4 edge and Ni L_3 edge, the magnetic moment for Ni could not be estimated from the analysis of Ni XMCD[58].

Figure 5(a)–(c) display the XMCD spectra of the *RE* cations Nd, Sm, and Gd, measured under the same conditions (6 T, 2 K). We now focus on the sign of the leading edge of these *RE* sites, with respect to the Ni/Mn XMCD signals, to understand the relative coupling between the *RE* and Ni/Mn sublattice. Our observations reveal that the leading edge of the Gd XMCD signal is negative in sign, implying its ferromagnetic alignment w.r.t the Ni/Mn sublattice as well as the field. On the contrary, the sign of the leading edge of both Nd and Sm are positive, implying that their m_s is aligned antiparallel to the Ni/Mn sublattice as well as the applied field. At first glance, it may seem unusual how Nd and Sm moments seem antiparallel even under such a high magnetic field. This observation can be explained by recalling that the effective magnetic moment of RE^{3+} ions is a spin-orbit coupled moment rather than a purely spin-derived one.

Now to understand the alignment of the net spin-orbit coupled moment, we note that both Nd^{3+} and Sm^{3+} possess less than half-filled 4*f* shells (Table 1), for which the total angular momentum is given by $J = |L - S|$. Consequently, their spin and orbital moments are intrinsically antiparallel, with the orbital contribution dominating. As a result, although the m_s appears antiparallel to the Ni/Mn sublattice, the total *RE* moment aligns parallel to it[41,63,79]. In contrast, Gd^{3+} has L = 0 (Table 1), leading to a purely spin-only magnetic moment that aligns parallel to the Ni/Mn sublattice, as observed in Fig. 5c. We further note that La^{3+} and Y^{3+} are non-magnetic.

Taken together, the XMCD results demonstrated by Fig. 5 establishes that under a high applied field, there is progressive net alignment of the net spin-orbit coupled moments of RE^{3+} in the direction of the field. This provides a microscopic explanation for the non-saturating behavior of the *M*–*H* curves at high magnetic fields [Fig. 4(a)], where increasing *H* gradually enforces ferromagnetic alignment of the *RE* sublattice with the transition-metal framework.

While high magnetic fields favor an overall parallel alignment of all magnetic sublattices, the low-field regime may reveal intriguing features. In RE_2NiMnO_6 compounds with *RE* = Nd and Sm, when the applied field is weaker than a compensation threshold, it is well established that it cannot overcome the internal exchange field of the *RE* sublattice. Under these conditions, these *RE* moments align antiferromagnetically with respect to the Ni-Mn sublattice, manifesting as a reduction of the net magnetization upon cooling in the $M - T$[41,80,81]. Although such signatures are not explicitly observed in our case, owing to the dominant contribution from Gd that masks the possibility of such a downturn, the *RE* sublattice still provides a competing space of magnetic interactions at these low fields. Thus, investigating the low-field behavior of our system under such *RE*-site compositional complexity will be particularly interesting.

Reentrant spin glass-like behavior

We next examine the low field, low temperature regime, which also indicated towards the possibility of a reentrant spin-glass state[40,82] from our $M - T$ measurements [Fig. 2(c)–(e)]. To experimentally verify this, we performed memory experiments to capture any glassy behavior at lower temperatures under a small applied field. When a spin glass system is quenched from a temperature above the glassy transition (T_g) down to a temperature lower than that, and then halted for a significant waiting time, aging effect is expected to be visible[35,40,83]. Following this protocol, the zero-field-cooled (ZFC) magnetization was first recorded during warming in a small magnetic field (H_{DC} ~ 50 Oe), following a continuous cooling from a temperature well above T^* down to the base temperature. A second ZFC measurement was then performed with an intermediate halt (T_{halt}) at ~10 K, i.e. below T^*, where the sample was held for a halt time of t_{halt} = 3000 sec before resuming the cooling [See Fig. 6(a) for the schematic of the protocol]. In both protocols, the magnetic field remained zero throughout the cooling and waiting processes. A pronounced cusp appears near 10 K in the aged curve (which is the halting temperature marked by *) in comparison to the non-aged curve. The inset shows the difference curve given by, $\Delta M = M_{3000sec} - M_{nowait}$ showing a 'memory dip' [Inset Fig. 6(b)]. This irreversibility behavior from aging experiments is a hallmark signature for spin glass states[35,40,83]. Since the system is magnetically ordered at a higher temperature (T_c), the data imply a reentrant spin-glass-like phase below T^*[40,82].

Discussions

We explore the potential sources of magnetic frustration that lead to the reentrant spin-glass-like phase. The presence of ASD in RE_2NiMnO_6 introduces additional antiferromagnetic couplings, specifically through Ni^{2+}-O-Ni^{2+} and Mn^{4+}-O-Mn^{4+} superexchange interactions[40,58]. These competing interactions coexist with the dominant ferromagnetic Ni^{2+}-O-Mn^{4+} superexchange. This competition between magnetic interactions is believed to be the origin of the reentrant spin-glass phase, which appears at approximately 100 K in La_2NiMnO_6 and Nd_2NiMnO_6 samples with

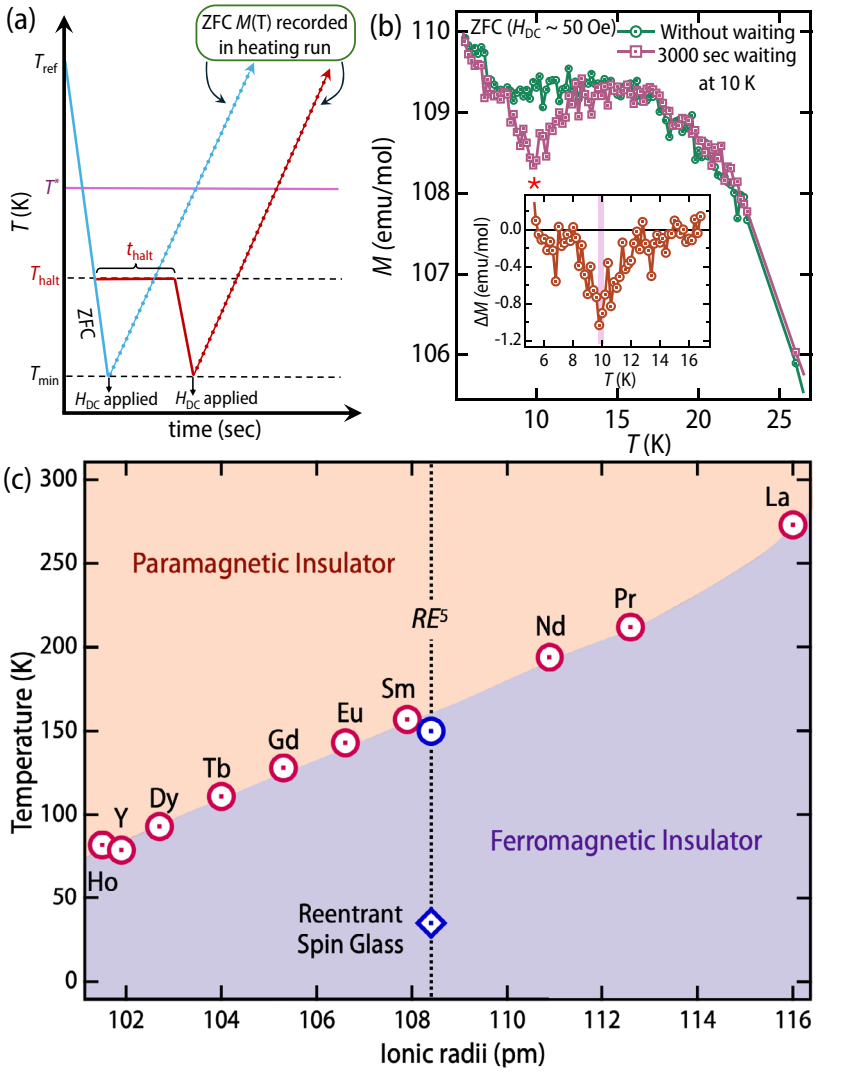

Fig. 6 | Memory experiment and magnetic phase diagram. a Temperature versus time schematic, demonstrating the cooling and heating processes for the memory experiment[93]. **b** ZFC magnetization recorded under H_{DC} = 50 Oe with and without halts at T = 10 K. Inset: Corresponding difference curves ΔM versus T (ZFC curve with halt minus curve without halt). **c** Magnetic phase diagram for RE_2NiMnO_6 compounds (RE = La, Pr, Nd, Sm, Eu, Gd, Tb, Dy, Y and Ho) highlighting the paramagnetic to ferromagnetic transition along with the results from our work for single crystalline RE^5NMO. T^* also has been additionally shown.

significant ASD[40,52–54]. At this temperature scale (~ 100 K), the magnetic interaction between the Ni/Mn sublattice and the Nd ions is considered negligible, as evidenced by the consistent temperature scale of this phase in both compounds, given that La is nonmagnetic. Additionally, La_2NiMnO_6 and Nd_2NiMnO_6 samples, prepared with very little ASD, do not exhibit a spin glass state[41,47,84]. On the other hand, the glassy phase appearing around 20 K in Sm_2NiMnO_6 has been described by the magnetic coupling of Sm^{3+} ion with Ni/Mn sublattice[81]. Furthermore, ASD induced spin glass states are often accompanied by exchange bias effects due to spin-glass/ferromagnetic phase coexistence[85,86]. Significantly, no exchange bias was observed in the present study [Supplementary Fig. S4]. This finding indicates the absence of magnetic phase separation, thereby suggesting that the spin-glass signature originates from the entire sample volume.

Interestingly, our M-T measurements reveal dynamical magnetic features below ~ 35 K, comparable to the RE-sublattice interaction temperature with the Ni/Mn sublattice. This suggests a second scenario in which disorder at the RE-site adds further complexity to both the nature and strength of the magnetic interactions. Given that the memory experiments were conducted at a low field of 50 Oe, any field-induced parallel alignment of Nd and Sm is unlikely. Instead, under such conditions, their net moments align antiferromagnetically with the Ni/Mn sublattice, as revealed by earlier reports on neutron diffraction on parent compounds[47,80]. This coupling further manifests as a downturn in magnetization at low temperatures in Nd_2NiMnO_6 and Sm_2NiMnO_6[41,78]. However, in our system, such a downturn trend is overcome by the strong paramagnetic response of the Gd, leading to an upturn in magnetization with lowering of temperature[46]. Overall, the RE sublattice via its coupling to the Ni/Mn network creates a complex landscape of competing magnetic interactions, varying in both nature and strength.

While both of the above mechanisms may jointly contribute to the glassy behavior, the markedly lower transition temperature observed here differs from the values reported for purely ASD-driven spin-glass states in the parent compounds. Figure 6(c) summarizes our observations, showing that the ferromagnetic transition in our system aligns with the general magnetic phase diagram of RE_2NiMnO_6 compounds. The average ionic size remains a reliable predictor of T_c even in this high variance compositionally complex settings, while a glassy phase appears at lower temperatures coinciding with the temperature scale of RE-sublattice interactions.

Conclusions and Outlook

In this study, we demonstrated that long-range ferromagnetic order can robustly persist in a high variance compositionally complex DPO $(La_{0.4}Nd_{0.4}Sm_{0.4}Gd_{0.4}Y_{0.4})NiMnO_6$. Our results demonstrate that the ferromagnetic transition temperature is primarily governed by the average ionic radius rather than the degree of variance, aligning with the mean-field scenario. Below T_c, the phonon frequency does not follow the expected anharmonic trend; instead, a mean-field-based phonon renormalization prevailed. However, a deviation from this mean-field behavior and the emergence of a reentrant spin-glass-like anomaly were observed, which was further confirmed by magnetic memory experiments. Such frustration may arise from both Ni/Mn antisite disorder and RE-site disorder; however, the

temperature of appearance of spin-glass-like anomaly is closer to the *RE*-Ni/Mn interaction scale, which points towards the *RE*-site exchange disorder as a possibly dominant driver in this case.

Overall, this work opens a pathway for designer ferromagnetic high-entropy materials for the targeted magnetic transition temperature. Considering the known appearance of a ferroelectric phase at the T_c in Y_2NiMnO_6[42], future research could focus on investigating the local structure of $RE^5_2NiMnO_6$ using advanced techniques like electron microscopy[48]. This would provide valuable insights into the potential for magnetoelectric and multiferroic functionalities of this new class of materials.

Methods

Sample preparation and characterization

Polycrystalline target of RE^5NMO was synthesized using solid state synthesis reaction by mixing stoichiometric quantities of La_2O_3, Nd_2O_3, Sm_2O_3, Gd_2O_3, Y_2O_3, NiO and MnO_2. The mixture was heated multiple times with intermediate grinding, with a final heating at 1300 °C. The powder was pressed into a pellet and sintered to yield the target for PLD growth.

Single crystalline films of RE^5NMO (thicknesses 6 and 100 nm) were grown on TiO_2-terminated $SrTiO_3$ [001] substrates acquired from Shikosha, Japan, using a Neocera-based PLD system. A KrF excimer laser operating at λ = 248 nm with a fluence of 2 J/cm^2 and repetition rate 2 Hz was used, and the growth was monitored via an in-situ reflection high-energy electron diffraction (RHEED) setup from Staib instruments [See Supplementary Note 1 for details on RHEED images]. The films were grown at a deposition temperature of 750 °C at a partial oxygen pressure of 150 mTorr. The films were annealed post-growth at 500 Torr for 30 minutes at the deposition temperature to prevent the formation of unwanted Mn^{3+}[57,59].

Post-characterization of the films was performed with XRD and XRR measurements using a lab-based Rigaku X-ray diffractometer, and the XRR fitting was carried out using GenX software[87]. For the grazing-incidence geometry used in the XRR measurement, the fitting was carried out after incorporating the footprint correction[88]. Diffuse reflectance spectra of the film were recorded using a Perkin Elmer LAMBDA UV-Vis spectrophotometer to determine the optical band gap.

XAS and XMCD measurements

XAS measurements at Ni $L_{3,2}$, Mn $L_{3,2}$ edges were carried out at beamline P04 PETRA III, DESY, Hamburg, Germany. The spectra were collected at room temperature in surface sensitive total electron yield (TEY) mode at grazing incidence geometry (angle of incidence ~ 20°). XMCD measurements with circularly polarized X-rays were performed at the Ni $L_{3,2}$, Mn $L_{3,2}$, Nd $M_{4,5}$, Sm $M_{4,5}$, and Gd $M_{4,5}$ edges at the BOREAS beamline, ALBA, Barcelona, Spain. The spectra were recorded at 2 K under the TEY mode. A magnetic field of 6 Tesla was applied parallel to the incident beam at grazing incidence.

Magnetic measurements

DC magnetization measurements were carried out using an MPMS XL superconducting quantum interference device (SQUID) magnetometer from Quantum Design Inc.

Raman measurements

Temperature-dependent Raman spectroscopy measurements were performed using Oxford-WITec Alpha 300R confocal photoluminescence Raman spectromicroscope in the 4 K to 300 K temperature range using liquid Helium. A laser wavelength of 532 nm and 1800 rules/mm grating was used to record the spectra in the wavenumber range of 100 to 850 cm^{-1}.

Data availability

All data are available from the corresponding authors, Srimanta Middey and Nandana Bhattacharya, upon reasonable request.

Received: 5 September 2025; Accepted: 5 March 2026;
Published online: 24 March 2026

References

1. Coey, J. M.*Magnetism and magnetic materials* (Cambridge University Press, 2010).
2. Feng, Z. et al. An anomalous Hall effect in altermagnetic ruthenium dioxide. *Nat. Electron.* **5**, 735–743 (2022).
3. Song, C. et al. Altermagnets as a new class of functional materials. *Nat. Rev. Mater.* **10**, 473–485 (2025).
4. Binder, K. & Young, A. P. Spin glasses: Experimental facts, theoretical concepts, and open questions. *Rev. Mod. Phys.* **58**, 801 (1986).
5. Broholm, C. et al. Quantum spin liquids. *Science* **367**, eaay0668 (2020).
6. Tokura, Y. Critical features of colossal magnetoresistive manganites. *Rep. Prog. Phys.* **69**, 797 (2006).
7. Wang, L. et al. Ferroelectrically tunable magnetic skyrmions in ultrathin oxide heterostructures. *Nat. Mater.* **17**, 1087–1094 (2018).
8. Nagaosa, N., Sinova, J., Onoda, S., MacDonald, A. H. & Ong, N. P. Anomalous hall effect. *Rev. Mod. Phys.* **82**, 1539–1592 (2010).
9. Vistoli, L. et al. Giant topological Hall effect in correlated oxide thin films. *Nat. Phys.* **15**, 67–72 (2019).
10. Ojha, S. K. et al. Oxygen vacancy-induced topological Hall effect in a nonmagnetic band insulator. *Adv. Quantum Technol.* **3**, 2000021 (2020).
11. Bhattacharya, A. & May, S. J. Magnetic oxide heterostructures. *Annu. Rev. Mater. Res.* **44**, 65–90 (2014).
12. Hellman, F. et al. Interface-induced phenomena in magnetism. *Rev. Mod. Phys.* **89**, 025006 (2017).
13. Rost, C. M. et al. Entropy-stabilized oxides. *Nat. Commun.* **6**, 8485 (2015).
14. Mazza, A. R. et al. Embracing disorder in quantum materials design. *Appl. Phys. Lett.* **124**, 230501 (2024).
15. Aamlid, S. S., Oudah, M., Rottler, J. & Hallas, A. M. Understanding the role of entropy in high entropy oxides. *J. Am. Chem. Soc.* **145**, 5991–6006 (2023).
16. Han, L. et al. Multifunctional high-entropy materials. *Nat. Rev. Mater.* **9**, 846–865 (2024).
17. Schweidler, S. et al. High-entropy materials for energy and electronic applications. *Nat. Rev. Mater.* **9**, 266–281 (2024).
18. Almishal, S. S. I. et al. Chemically-disordered transparent conductive perovskites with high crystalline fidelity. *Adv. Sci.* **12**, e09868 (2025).
19. Yoo, S. et al. Efficient data processing using tunable entropy-stabilized oxide memristors. *Nat. Electron.* **7**, 466–474 (2024).
20. Niculescu, G. E. et al. Local structure maturation in high entropy oxide $(Mg,Co,Ni,Cu,Zn)_{1-x}(Cr,Mn)_xO$ thin films. *J. Am. Ceram. Soc.* **108**, e20171 (2025).
21. Miao, L. et al. Chemical environment and structural variations in high entropy oxide thin film probed with electron microscopy. *ACS Nano* **18**, 14968–14977 (2024).
22. Brahlek, M. et al. Unexpected crystalline homogeneity from the disordered bond network in $La(Cr_{0.2}Mn_{0.2}Fe_{0.2}Co_{0.2}Ni_{0.2})O_3$ films. *Phys. Rev. Mater.* **4**, 054407 (2020).
23. Mazza, A. R. et al. Variance induced decoupling of spin, lattice, and charge ordering in perovskite nickelates. *Phys. Rev. Res.* **5**, 013008 (2023).
24. Zhao, Z. et al. Strained single crystal high entropy oxide manganite thin films. *Appl. Phys. Lett.* **125**, 011902 (2024).
25. Witte, R. et al. High-entropy oxides: An emerging prospect for magnetic rare-earth transition metal perovskites. *Phys. Rev. Mater.* **3**, 034406 (2019).
26. Mazza, A. R. et al. Designing magnetism in high entropy oxides. *Adv. Sci.* **9**, 2200391 (2022).
27. Mazza, A. R. et al. Charge doping effects on magnetic properties of single-crystal $La_{1-x}Sr_x(Cr_{0.2}Mn_{0.2}Fe_{0.2}Co_{0.2}Ni_{0.2})O_3$ ($0 \le x \le 0.5$) high-entropy perovskite oxides. *Phys. Rev. B* **104**, 094204 (2021).
28. Sarkar, A. et al. High entropy approach to engineer strongly correlated functionalities in manganites. *Adv. Mater.* **35**, 2207436 (2023).

29. Ke, W.-E. et al. Crystalline magnetic anisotropy in high entropy (Fe, Co, Ni, Cr, Mn)$_3$O$_4$ oxide driven by single-element orbital anisotropy. *Adv. Funct. Mater.* **34**, 2312856 (2024).
30. Zhang, J. et al. Long-range antiferromagnetic order in a rocksalt high entropy oxide. *Chem. Mater.* **31**, 3705–3711 (2019).
31. Jimenez-Segura, M. P. et al. Long-range magnetic ordering in rocksalt-type high-entropy oxides. *Appl. Phys. Lett.* **114**, 122401 (2019).
32. Nevgi, R. et al. Local structural distortions drive magnetic molecular field in compositionally complex spinel oxide. *Nat. Commun.* **16**, 7038 (2025).
33. Min, L. et al. High entropy protected sharp magnetic transitions in highly disordered spinel ferrites. *J. Am. Chem. Soc.* **146**, 24320–24329 (2024).
34. Clulow, R. et al. Phase stability and magnetic properties of compositionally complex n = 2 Ruddlesden-Popper perovskites. *Inorg. Chem.* **63**, 6616–6625 (2024).
35. Pramanik, P. et al. Spin glass states in multicomponent layered perovskites. *Sci. Rep.* **14**, 3382 (2024).
36. Middey, S., Bhattacharya, N., Nevgi, R., Joshi, S. C., & Dey, S. Extreme compositional complexity in crystalline perovskite oxide: a new paradigm in quantum materials research. *Adv. Phys.: X.*, **11**, 2646243 (2026).
37. Blundell, S. *Magnetism in condensed matter* (OUP Oxford, 2001).
38. Vasala, S. & Karppinen, M. $A_2B'B''O_6$ perovskites: A review. *Prog. Solid State Chem.* **43**, 1–36 (2015).
39. Rogado, N. S., Li, J., Sleight, A. W. & Subramanian, M. A. Magnetocapacitance and magnetoresistance near room temperature in a ferromagnetic semiconductor: La_2NiMnO_6. *Adv. Mater.* **17**, 2225–2227 (2005).
40. Choudhury, D. et al. Near-room-temperature colossal magnetodielectricity and multiglass properties in partially disordered La_2NiMnO_6. *Phys. Rev. Lett.* **108**, 127201 (2012).
41. Pal, S. et al. Peculiar magnetic states in the double perovskite Nd_2NiMnO_6. *Phys. Rev. B* **100**, 045122 (2019).
42. Su, J. et al. Magnetism-driven ferroelectricity in double perovskite Y_2NiMnO_6. *ACS Appl. Mater. Interfaces* **7**, 13260–13265 (2015).
43. Nasir, M. et al. Role of antisite disorder, rare-earth size, and superexchange angle on band gap, curie temperature, and magnetization of R_2NiMnO_6 double perovskites. *ACS Appl. Electron. Mater.* **1**, 141–153 (2019).
44. Li, D. et al. Emergent and robust ferromagnetic-insulating state in highly strained ferroelastic $LaCoO_3$ thin films. *Nat. Commun.* **14**, 3638 (2023).
45. Li, T. et al. Room-temperature perovskite ferromagnetic insulator via three-dimensional tensile strain. *Phys. Rev. Lett.* **134**, 016702 (2025).
46. Booth, R. et al. An investigation of structural, magnetic and dielectric properties of R_2NiMnO_6 (R= rare earth, Y). *Mater. Res. Bull.* **44**, 1559–1564 (2009).
47. Sanchez-Benitez, J., Martinez-Lope, M., Alonso, J. & Garcia-Munoz, J. Magnetic and structural features of the $NdNi_{1-x}Mn_xO_3$ perovskite series investigated by neutron diffraction. *J. Phys.: Condens. Matter* **23**, 226001 (2011).
48. Bhattacharya, N. et al. Nanoscale inhomogeneity and epitaxial strain control metallicity in single crystalline thin films of high entropy oxide. *Adv. Mater.* **37**, 2418490 (2025).
49. Patel, R. K. et al. Epitaxial stabilization of ultra-thin films of high entropy perovskite. *Appl. Phys. Lett.* **116**, 071601 (2020).
50. Patel, R. K. et al. Thickness dependent oer electrocatalysis of epitaxial thin film of high entropy oxide. *Appl. Phys. Rev.* **10**, 031407 (2023).
51. Iliev, M., Guo, H. & Gupta, A. Raman spectroscopy evidence of strong spin-phonon coupling in epitaxial thin films of the double perovskite La_2NiMnO_6. *Appl. Phys. Lett.* **90** (2007).
52. Shi, C., Hao, Y. & Hu, Z. Local valence and physical properties of double perovskite Nd_2NiMnO_6. *J. Phys. D: Appl. Phys.* **44**, 245405 (2011).
53. Iliev, M. et al. Growth, magnetic properties, and raman scattering of La_2NiMnO_6 single crystals. *J. Appl. Phys.* **106**, 023515 (2009).
54. Singh, A. K., Chauhan, S., Srivastava, S. K. & Chandra, R. Influence of antisite disorders on the magnetic properties of double perovskite Nd_2NiMnO_6. *Solid State Commun.* **242**, 74–78 (2016).
55. Tauc, J., Grigorovici, R. & Vancu, A. Optical properties and electronic structure of amorphous germanium. *phys. stat. sol. (b)* **15**, 627–637 (1966).
56. Das, H., Waghmare, U. V., Saha-Dasgupta, T. & Sarma, D. Electronic structure, phonons, and dielectric anomaly in ferromagnetic insulating double pervoskite La_2NiMnO_6. *Phys. Rev. Lett.* **100**, 186402 (2008).
57. Bhattacharya, N. et al. Site-selective polar compensation of mott electrons in a double-perovskite heterointerface. *Phys. Rev. Lett.* **134**, 176201 (2025).
58. Pal, S. et al. Effect of anti-site disorder on magnetism in La_2NiMnO_6. *Phys. Rev. B* **97**, 165137 (2018).
59. Bhattacharya, N. et al. Interfacial reconstruction effects in insulating double perovskite $Nd_2NiMnO_6/SrTiO_3$ and $Nd_2NiMnO_6/NdGaO_3$ thin films. *Phys. Rev. B* **111**, 235438 (2025).
60. Pesquera, D. et al. Surface symmetry-breaking and strain effects on orbital occupancy in transition metal perovskite epitaxial films. *Nat. Commun.* **3**, 1189 (2012).
61. Pesquera, D. et al. Strain-driven orbital and magnetic orders and phase separation in epitaxial half-doped manganite films for tunneling devices. *Phys. Rev. Appl.* **6**, 034004 (2016).
62. Zenia, H., Gehring, G. A., Banach, G. & Temmerman, W. M. Electronic and magnetic properties of the (001) surface of hole-doped manganites. *Phys. Rev. B* **71**, 024416 (2005).
63. Spring, J. et al. Paramagnetic Nd sublattice and thickness-dependent ferromagnetism in Nd_2NiMnO_6 double perovskite thin films. *Phys. Rev. Mater.* **7**, 104407 (2023).
64. Mugiraneza, S. & Hallas, A. M. Tutorial: a beginner's guide to interpreting magnetic susceptibility data with the Curie-Weiss law. *Commun. Phys.* **5**, 95 (2022).
65. Guo, H., Gupta, A., Calvarese, T. & Subramanian, M. Structural and magnetic properties of epitaxial thin films of the ordered double perovskite La_2CoMnO_6. *Appl. Phys. Lett.* **89**, 262503 (2006).
66. Carlin, R. L. *Magnetochemistry* (Springer Science & Business Media, 2012).
67. Iliev, M. et al. Raman spectroscopy of ordered double perovskite La_2CoMnO_6 thin films. *Phys. Rev. B* **75**, 104118 (2007).
68. Macedo Filho, R. et al. Role of rare-earth ionic radii on the spin–phonon coupling in multiferroic ordered double perovskites. *Mater. Res. Express* **2**, 075201 (2015).
69. Laverdière, J. et al. Spin-phonon coupling in orthorhombic $RMnO_3$ (R= Pr, Nd, Sm, Eu, Gd, Tb, Dy, Ho, Y): A Raman study. *Phys. Rev. B* **73**, 214301 (2006).
70. Haro, E., Balkanski, M., Wallis, R. & Wanser, K. Theory of the anharmonic damping and shift of the Raman mode in silicon. *Phys. Rev. B* **34**, 5358 (1986).
71. Granado, E. et al. Magnetic ordering effects in the Raman spectra of $La_{1-x}Mn_{1-x}O_3$. *Phys. Rev. B* **60**, 11879 (1999).
72. Truong, K., Singh, M., Jandl, S. & Fournier, P. Influence of Ni/Mn cation order on the spin-phonon coupling in multifunctional La_2NiMnO_6 epitaxial films by polarized Raman spectroscopy. *Phys. Rev. B* **80**, 134424 (2009).
73. van der Laan, G. et al. Experimental proof of magnetic x-ray dichroism. *Phys. Rev. B* **34**, 6529 (1986).
74. Vaz, C. et al. X-ray magnetic circular dichroism. *Nat. Rev. Methods Primers* **5**, 27 (2025).
75. Van der Laan, G. & Figueroa, A. I. X-ray magnetic circular dichroism—a versatile tool to study magnetism. *Coord. Chem. Rev.* **277**, 95–129 (2014).
76. Carra, P., Thole, B., Altarelli, M. & Wang, X. X-ray circular dichroism and local magnetic fields. *Phys. Rev. Lett.* **70**, 694 (1993).

77. Piamonteze, C., Miedema, P. & De Groot, F. M. Accuracy of the spin sum rule in XMCD for the transition-metal L edges from manganese to copper. *Phys. Rev. B* **80**, 184410 (2009).
78. Majumder, S. et al. Mapping the magnetic state as a function of antisite disorder in Sm_2NiMnO_6 double perovskite thin films. *Phys. Rev. B* **105**, 024408 (2022).
79. Spring, J. et al. Engineering the magnetic transition temperatures and the rare earth exchange interaction in oxide heterostructures. *ACS Nano* **19**, 14652–14660 (2025).
80. Majumder, S. et al. Microscopic insights of magnetism in Sm_2NiMnO_6 double perovskite. *Phys. Rev. B* **105**, 094425 (2022).
81. Lekshmi, P. N. et al. Re-entrant spin glass behaviour and magneto-dielectric effect in insulating Sm_2NiMnO_6 double perovskite. *J. Mater. Chem. C.* **1**, 6565–6574 (2013).
82. Kumar, P. A. et al. Reentrant superspin glass phase in a $La_{0.82}Ca_{0.18}MnO_3$ ferromagnetic insulator. *Phys. Rev. X* **4**, 011037 (2014).
83. Mathieu, R., Jönsson, P., Nam, D. & Nordblad, P. Memory and superposition in a spin glass. *Phys. Rev. B* **63**, 092401 (2001).
84. Yang, W., Liu, X., Zhao, H., Lin, Y. & Chen, X. Structure, magnetic, and dielectric characteristics of Ln_2NiMnO_6 (Ln= Nd and Sm) ceramics. *J. Appl. Phys.* **112**, 064104 (2012).
85. Wang, X. et al. The influence of the antiferromagnetic boundary on the magnetic property of La_2NiMnO_6. *Appl. Phys. Lett.* **95**, 252502 (2009).
86. Singh, A. K., Chauhan, S. & Chandra, R. Antisite disorder induced spin glass and exchange bias effect in Nd_2NiMnO_6 epitaxial thin film. *Appl. Phys. Lett.* **110**, 102402 (2017).
87. Björck, M. & Andersson, G. Genx: An extensible x-ray reflectivity refinement program utilizing differential evolution. *J. Appl. Cryst.* **40**, 1174–1178 (2007).
88. Gibaud, A., Vignaud, G. & Sinha, S. The correction of geometrical factors in the analysis of X-ray reflectivity. *Acta Cryst. A* **49**, 642–648 (1993).
89. Shannon, R. D. Revised effective ionic radii and systematic studies of interatomic distances in halides and chalcogenides. *Acta Cryst. A* **32**, 751–767 (1976).
90. López, R. & Gómez, R. Band-gap energy estimation from diffuse reflectance measurements on sol–gel and commercial TiO_2: a comparative study. *J. Sol.-Gel Sci. Technol.* **61**, 1–7 (2012).
91. Arima, T., Tokura, Y. & Torrance, J. Variation of optical gaps in perovskite-type 3d transition-metal oxides. *Phys. Rev. B* **48**, 17006 (1993).
92. Yi, K., Tang, Q., Wu, Z. & Zhu, X. Unraveling the structural, dielectric, magnetic, and optical characteristics of nanostructured La_2NiMnO_6 double perovskites. *Nanomaterials* **12**, 979 (2022).
93. Joshi, D. C., Gebresenbut, G., Gomez, C. P. & Mathieu, R. Memory and rejuvenation in a quasicrystal. *EPL* **132**, 27002 (2020).

Acknowledgements

NB and SM thank Dr. Subhadeep Datta for insightful discussions on Raman spectroscopy data analysis. The authors acknowledge the use of central facilities of the Department of Physics, IISc, funded through the FIST program of the Department of Science and Technology (DST), Gov. of India. SM acknowledges funding support from a SERB Core Research grant (Grant No. CRG/2022/ 001906) and a DST Nano Mission consortium project (No. DST/NM/TUE/QM-5/2019). RKD and RM thank the Olle Engkvist Stiftelse (Grant No. 224-0046) for financial support. NB, SD acknowledge support from the Prime Minister's Research Fellowship (PMRF), MoE, Government of India. NB also thanks Shakipriya Patra for assistance with solid-state synthesis.

Author contributions

S.M. conceived and supervised the project. N.B. performed the synthesis, thin film growth, characterization, and Raman experiments with the help of S.J. and S.D. R.K.D. performed the magnetic measurements under the supervision of R.M. S.C., M.V., and M.H. performed the XAS and XMCD measurements. N.B. performed all analyses with inputs from S.M., R.M., R.K.D., and SC. N.B. and S.M. wrote the manuscript with inputs from all authors.

Competing interests

The authors declare no competing interests.

Additional information

Supplementary information The online version contains supplementary material available at https://doi.org/10.1038/s43246-026-01135-8.

Correspondence and requests for materials should be addressed to Nandana Bhattacharya or Srimanta Middey.

Peer review information *Communications Materials* thanks the anonymous reviewers for their contribution to the peer review of this work.